nature materials

Article

https://doi.org/10.1038/s41563-022-01364-5

Topological Lifshitz transition and one-dimensional Weyl mode in $HfTe_5$

Received: 30 January 2022

Accepted: 15 August 2022

Published online: 29 September 2022

Check for updates

Wenbin Wu[1,11], Zeping Shi[1,11], Yuhan Du[1], Yuxiang Wang[2], Fang Qin[3], Xianghao Meng[1], Binglin Liu[1], Yuanji Ma[1], Zhongbo Yan[4], Mykhaylo Ozerov[5], Cheng Zhang[2,6] ✉, Hai-Zhou Lu[3,7], Junhao Chu[8,9,10] and Xiang Yuan[1,8] ✉

Landau band crossings typically stem from the intra-band evolution of electronic states in magnetic fields and enhance the interaction effect in their vicinity. Here in the extreme quantum limit of topological insulator $HfTe_5$, we report the observation of a topological Lifshitz transition from inter-band Landau level crossings using magneto-infrared spectroscopy. By tracking the Landau level transitions, we demonstrate that band inversion drives the zeroth Landau bands to cross with each other after 4.5 T and forms a one-dimensional Weyl mode with the fundamental gap persistently closed. The unusual reduction of the zeroth Landau level transition activity suggests a topological Lifshitz transition at 21 T, which shifts the Weyl mode close to the Fermi level. As a result, a broad and asymmetric absorption feature emerges due to the Pauli blocking effect in one dimension, along with a distinctive negative magneto-resistivity. Our results provide a strategy for realizing one-dimensional Weyl quasiparticles in bulk crystals.

In magnetic fields, electrons in crystals undergo cyclotron motion and transform the energy bands into discrete Landau levels. The formation of Landau levels gives rise to various phenomena such as Shubnikov–de Haas oscillations and integer and fractional quantum Hall effects, as well as composite fermions[1–3]. In two-dimensional (2D) systems like graphene and quantum wells, these Landau levels are non-dispersive. When additional energy such as spin or valley splitting exceeds the cyclotron energy, Landau levels meet with each other at critical magnetic fields, and electron interaction is enhanced as a result[4]. This type of intra-band Landau level crossing, which comes from the overlap of energy levels without dispersion, has been widely investigated and serves as an essential tool to modulate and analyse the Landau level spectrum[5–8]. By contrast, Landau levels in three-dimensional (3D) systems change into Landau bands due to the dispersion along the magnetic field direction. As the field varies, the evolution of the cyclotron energy and band splitting potentially lead to the Landau band crossings existing only at discrete momentums. If one is considering an inverted-band system such as a weak topological insulator (TI), the spin splitting drives the lowest (zeroth) Landau bands of the conduction and valence bands moving towards each other and finally crossing above a critical magnetic field at discrete momentums. Hereafter, the 'inter-band Landau level crossing' denotes the crossing between conduction and valence Landau levels in momentum space. Notably, such inter-band Landau level crossings persistently close the fundamental bandgap rather than the Landau gap alone. The further increased magnetic field only shifts the crossing momentums but keeps the bandgap closed.

On the other hand, band crossing in momentum space generates quasiparticles, which has drawn enormous research interest. The most

[1]State Key Laboratory of Precision Spectroscopy, East China Normal University, Shanghai, China. [2]State Key Laboratory of Surface Physics and Institute for Nanoelectronic Devices and Quantum Computing, Fudan University, Shanghai, China. [3]Shenzhen Institute for Quantum Science and Engineering and Department of Physics, Southern University of Science and Technology (SUSTech), Shenzhen, China. [4]School of Physics, Sun Yat-Sen University, Guangzhou, China. [5]National High Magnetic Field Laboratory, Florida State University, Tallahassee, FL, USA. [6]Zhangjiang Fudan International Innovation Center, Fudan University, Shanghai, China. [7]Shenzhen Key Laboratory of Quantum Science and Engineering, Shenzhen, China. [8]School of Physics and Electronic Science, East China Normal University, Shanghai, China. [9]Key Laboratory of Polar Materials and Devices, Ministry of Education, East China Normal University, Shanghai, China. [10]Institute of Optoelectronics, Fudan University, Shanghai, China. [11]These authors contributed equally: Wenbin Wu, Zeping Shi. ✉e-mail: zhangcheng@fudan.edu.cn; xyuan@lps.ecnu.edu.cn

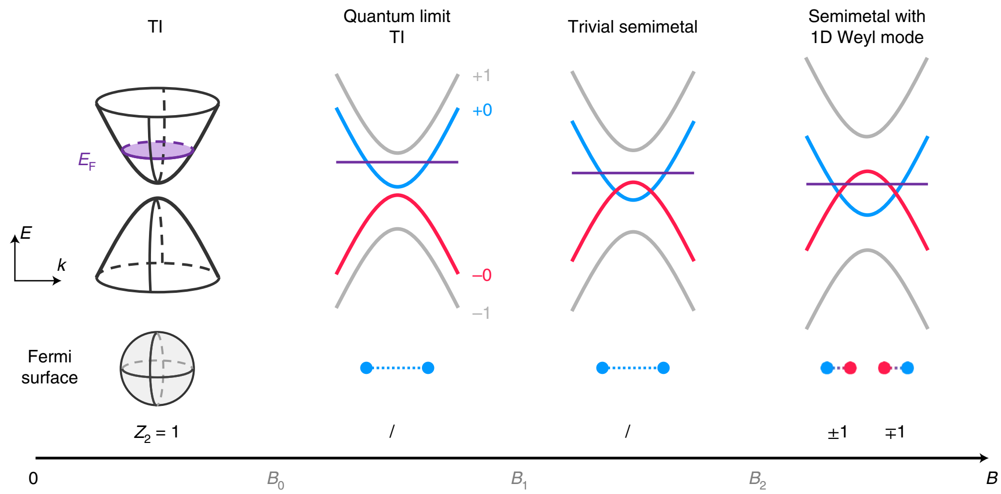

Fig. 1 | Schematic plot of proposed magnetic-field-driven phase transitions. A weak 3D TI at zero field with $\Delta > 0$, $M < 0$ and $M_z > 0$. The Landau quantization of the TI features both band inversion and full spin-polarization of the zeroth Landau bands, denoted by red and blue lines, while the black and grey lines denote the original energy bands and high-index Landau bands, respectively. After reaching the quantum limit at B_0, the Fermi level (purple) crosses only the zeroth Landau band. Characteristic band inversion leads to the crossing of the zeroth Landau bands after the critical field of B_1. With the Fermi level staying high, the system still behaves as a trivial semimetal until the Lifshitz transition at B_2. Fermi surfaces experience a splitting, which is accompanied by a topological transition where the zeroth Landau bands form an effective 1D and spin-polarized band crossing near the Fermi energy (E_F).

cited examples involve the Dirac equation, which can be simplified into two massless Weyl equations[9]. By breaking either inversion or time reversal symmetry and forming a band crossing, a Weyl fermion has been theoretically proposed and experimentally realized[10–14]. This success offers a platform to study the chiral fermion and leads to the discovery of a chiral anomaly and other unique electromagnetic responses[15–24]. The discussed inter-band Landau level crossings from TI lead to the effective one-dimensional (1D) structure without geometry confinement, as the magnetic field erases the in-plane dispersion. The 1D crossing mimics both the electronic structure and spin texture of the Weyl nodes formed by the Bloch band crossing, which is defined as '1D Weyl mode' in the following. However, the effective Zeeman energy is generally much smaller than the bandgap and the Fermi energy. Hence, the inter-band Landau level crossings, as well as the corresponding 1D Weyl mode in the quantum limit, remain largely unexplored.

Here we report evidence of a topological Lifshitz transition from inter-band Landau level crossings in the topological insulator $HfTe_5$. Due to the low Fermi energy, $HfTe_5$ reaches the quantum limit in a very low field of ~1.5 T. A series of Landau level resonances along with band splitting behaviour are revealed by magneto-infrared spectroscopy. By further ramping up the magnetic field, we observe a highly unusual reduction of optical activity from zeroth Landau level transitions in the extreme quantum limit, which indicates the topological Lifshitz transition and the formation of a 1D Weyl mode near the Fermi level. The electromagnetic response of this induced Weyl mode is revealed by both high-field optical and transport approaches, from which signatures of 1D Pauli blocking and negative magneto-resistivity are detected. The field-induced origin manifests a Weyl mode with an immense density of states (DOS) near the Fermi level, in stark contrast with the vanishing DOS in the 3D Weyl node.

Field-driven topological phase transitions and the 1D Weyl mode

Considering a weak 3D TI with an in-plane inverted gap, a series of magnetic-field-driven phase transitions are proposed at critical fields of B_0, B_1, B_2 as shown in Fig. 1. Applying a magnetic field (B) first leads to the formation of 1D Landau bands, which are parabolically dispersed along the field direction especially around the band edge at zero momentum. Once reaching the quantum limit at B_0, the Fermi level crosses only with the zeroth Landau band. By increasing the magnetic fields, band inversion drives the two zeroth Landau bands, moving towards and eventually forming inter-band crossings at B_1. At first, the Fermi level remains higher than the Lifshitz transition energy, so the system behaves as a trivial semimetal. Above B_2, a Lifshitz transition takes place accompanied by a topological phase transition with the Fermi surface divided into two parts with opposite spin textures. Such topological Lifshitz transitions originate from the dispersive Landau bands, and are different from those in the Bloch bands[25]. The non-zero topological number of each phase is denoted below the Fermi surface in Fig. 1. The 1D crossing analogue to the Weyl node formed by Bloch band crossing persists at higher magnetic fields. The overall phase transitions and main physics can be modelled by the ideal low-energy Hamiltonian[26]

$$H(\mathbf{k}) = \hbar v_{Fx} k_x \tau_x \sigma_z - \hbar v_{Fy} k_y \tau_y \sigma_0 + \hbar v_{Fz} k_z \tau_x \sigma_x + \left[\Delta + M\left(k_x^2 + k_y^2\right) + M_z k_z^2\right] \tau_z \sigma_0, \quad (1)$$

where $\mathbf{k}$ is the momentum, and τ and σ are the Pauli matrixes acting on the orbital and spin degrees of freedom, respectively. $\hbar$ and σ_0 are reduced Planck's constant and the unit matrix, respectively. The subscripts x, y, z correspond to the a, c, b crystal axis of the $HfTe_5$. Band parameters include the energy gap 2Δ, Fermi velocity v_F and, in-plane and out-of-plane band inversion parameters M and M_z. The Fermi velocity and band inversion parameters also act as linear and parabolic contributions of energy dispersion[27]. Influence from additional perturbation terms[28–30] such as spin–orbit coupling and inversion symmetry breaking are further discussed in Supplementary Section III.

Material realization and anisotropic band structure

Among various TI candidates, we find that $HfTe_5$ meets the material criteria to realize the above proposal. Similar to $ZrTe_5$, $HfTe_5$ is at the boundary between weak TI and strong TI[31–33], with the electronic structure and band topology sensitive to the b-axis lattice constant. The access to the extreme quantum limit has led to various intriguing phenomena in $ZrTe_5$ and $HfTe_5$ (refs. [34–39]). Photoemission and optical experiments reveal a temperature-dependent Fermi level and a TI phase at low temperature[40,41]. Figure 2a–d exhibits the quantum oscillations from our transport measurement. A large positive magneto-resistivity is observed with a small Fermi vector $k_{Fac} = 5.9 \times 10^{-3}$ Å, in agreement with

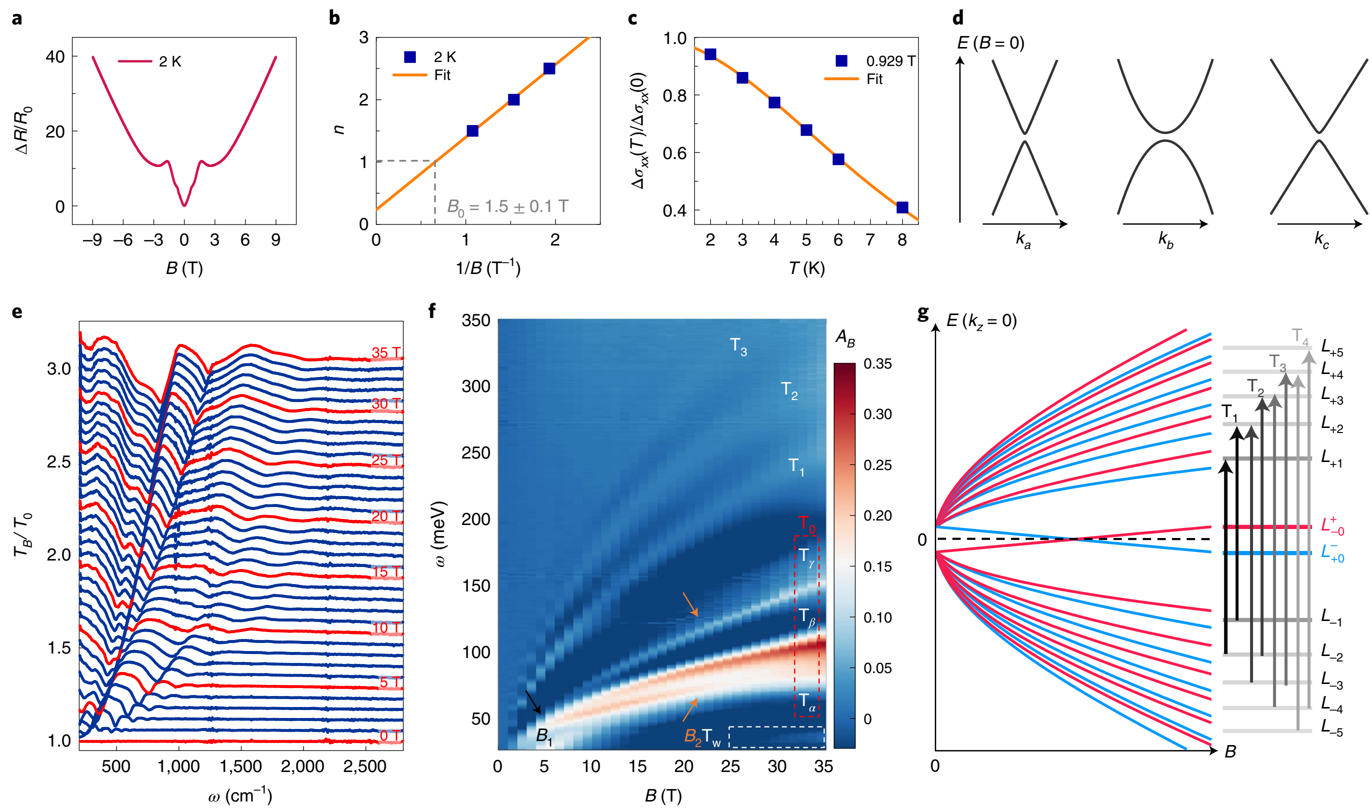

Fig. 2 | Band structure and magneto-infrared spectroscopy in $HfTe_5$. **a**, Magneto-resistivity showing a large ratio and quantum oscillation. ΔR, resistivity variation; R_0, original resistivity without magnetic field. **b**, Fan diagram exhibiting a small Fermi surface and quantum limit at $B_0 \approx 1.5$ T, indicated by the grey dashed lines. **c**, Temperature (T)-dependent normalized oscillation amplitude $\Delta\sigma_{xx}(T)/\Delta\sigma_{xx}(0)$. **d**, The conclusive anisotropic band structure of $HfTe_5$ for setting model parameters. **e**, Relative magneto-transmittance spectra T_B/T_0 at different magnetic fields. For clarification, curves are vertically stacked and further coloured to red with 5 T intervals. The Landau level transitions (dips) systematically evolve with the magnetic fields. **f**, False-colour plot of the magneto-absorbance $A_B = -\ln(T_B/T_0)$. The assignments of Landau level transitions are labelled as T_n. The black arrow points to the splitting features originating from the zeroth Landau band edge touching at the critical field of B_1. The orange arrows present the optical activity variation due to the Lifshitz transition and resultant formation of the Weyl mode near the Fermi level at the critical field of B_2. The white dashed box exhibits the optical features from the 1D Pauli blocking effect. **g**, The schematic Landau band edge energy of $HfTe_5$ under various magnetic field values. The arrows exhibit the non-zeroth Landau level transitions.

previous reports[42]. ΔR and R_0 denote the resitivity variation and original resistivity without magnetic field. The fitted quantum limit in our sample is around $B_0 = 1.5 \pm 0.1$ T. Assuming an ellipsoid Fermi surface[42], we can obtain the cyclotron mass from the temperature-dependent oscillation amplitude, as $m_a = 0.016m_e$, $m_b = 1.2m_e$ and $m_c = 0.028m_e$, where m_e is the free electron mass (details are in Supplementary Sections I and II). Small m_a and m_b values suggest quasi-linear in-plane dispersion, while m_b indicates a parabolic dispersion along k_b (Fig. 2d). Hence, we set the v_{Fz} term to be zero while M_z remains finite for $HfTe_5$ (ref. [37]). With positive Δ, the in-plane band inversion of the TI requires $M < 0$. As shown later, the sign of M_z determines the presence of inter-band Landau level crossings and a Lifshitz transition. The a–c plane is treated as isotropic because the cyclotron motion averages the in-plane response. The low carrier concentration along with the special anisotropic dispersion and band inversion serve as the prerequisites to observe the topological Lifshitz transition within a magnetic field of 35 T.

High-field magneto-infrared spectrum

The evolution of Landau bands is detected by magneto-infrared spectroscopy with optical transmittance T_B/T_0 (Fig. 2e) measured at the a–c plane of $HfTe_5$ under magnetic fields applied along the b axis (Faraday geometry). Here T_B and T_0 are the transmittance measured in magnetic field B and zero field, respectively. A series of absorption peaks develops and evolves with the magnetic fields as shown in the relative magneto-absorbance $A_B = -\ln(T_B/T_0)$ (Fig. 2f). For those optical transitions labelled as T_1, T_2, T_3..., the transition energy approximately follows $\omega \propto \left(\sqrt{n+1}+\sqrt{n}\right)\sqrt{B}$ with $n = 1, 2, 3...$, which indicates a Dirac-type band in $HfTe_5$. Since the joint DOS diverges at the band edge, we focus on the $k_z = 0$ case at this stage and start from the optical transitions with the non-zeroth Landau band described by Eq. (2). The Landau bands are labelled as L_n^s with $n = \pm0, \pm1, \pm2...$ and $s = \pm1$ denoting the Landau index and spin index, respectively. The zeroth ($|n| = 0$) Landau bands are fully spin-polarized, distinct from all others. Band inversion leads to a field-dependent energy shift, which is most prominent for the zeroth Landau bands. Figure 2g presents a schematic plot of the Landau band edge energy $E(k_z = 0)$ versus B. The red and blue lines in Figs. 2g and 3c denote spin-polarized Landau bands. The optical transitions between Landau bands are restricted by a selection rule of $\Delta|n| = \pm1$ for the ideal model. The photon energy for the T_n transition ($L_{-n} \to L_{n+1}$ and $L_{-(n+1)} \to L_n$) follows Eq. (5) in the Methods, by which the transition index is assigned accordingly. The extracted Fermi velocity with $v_{ac} = 4.58 \times 10^5$ m s^{-1} is consistent with transport measurement. The observed inter-Landau-level transitions give the same intercept at zero field, corresponding to a small bandgap of ~5 meV.

For optical transitions with energy lower than T_1 in Fig. 2f, they are readily seen to arise from the zeroth Landau bands. Here we name these three transitions T_α, T_β, T_γ with increasing energy and refer to them together as T_0. As the Fermi level drops below the band edge of L_{+1} at $B_0 \approx 1.5$ T, only the zeroth Landau bands are occupied so that the strength of the T_0 transition is much higher than T_1, as shown in Fig. 3a(i). When further increasing the magnetic field, L_{+0}^- and L_{-0}^+ come closer due to band inversion and eventually touch at the critical field

https://doi.org/10.1038/s41563-022-01364-5

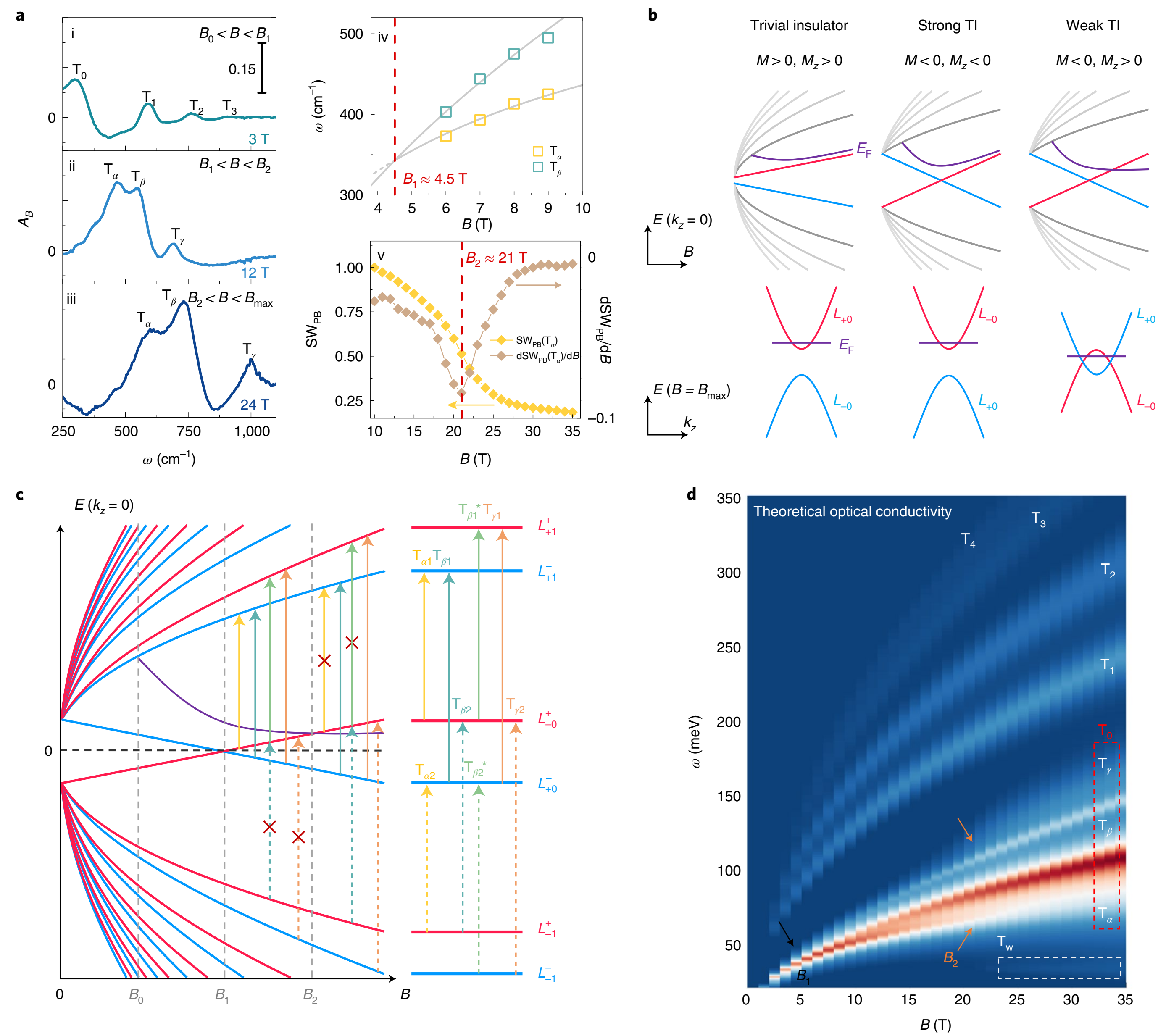

Fig. 3 | Optical activity of Landau level transitions and field-driven phase transitions. a, Relative magneto-absorbance spectra at different magnetic field regimes: after reaching the deep quantum limit at $B_0 < B < B_1$, showing T_0 as the most prominent transition with only the zeroth Landau band occupied (i); after the touching of the zeroth Landau band edge at $B_1 < B < B_2$, showing the split T_α and T_β indicating the crossing of the zeroth Landau bands (ii); and after the Lifshitz transition at $B > B_2$, showing the intensity reduction of T_α in contrast with the continuous intensity boost of T_β and T_γ, suggesting the emergence of a 1D Weyl mode near the Fermi level (iii). The fitted peak position in iv confirms the splitting behaviour, which agrees with the model (grey solid lines) and gives $B_1 \approx 4.5$ T (red dashed line). Grey dashed line denotes that T_α is not active below B_1. The normalized Pauli-blocking-induced spectral weight SW_{PB} of T_α and its first derivative in v prove the reduction of T_α and give $B_2 \approx 21$ T. **b**, Landau bands and Fermi level variation with magnetic field in small gap insulators with different topologies. In general cases, the Femi level does not cross any Landau band extrema after the quantum limit. An exception is presented in the weak TI where the Fermi level (in purple) crosses L_{-0}, which explains the unusual reduction of T_α and the 1D Weyl mode. **c**, Landau band extrema energy versus magnetic field, focusing on the T_0 transition. The activity of the optical transition is plotted by arrows with and without red crosses. $T_{\alpha1}$ in yellow experiences activity reduction through B_2 while $T_{\gamma2}$ experiences the opposite. **d**, Model prediction of the real part of the magneto-optical conductivity spectrum based on the fitting parameters, which reproduce the experimental features of inter-Landau-level transitions.

B_1. This touching results in the splitting of T_α and T_β as shown by Fig. 3a(ii),(iv) and the black arrow in Fig. 2f. The presence of small spin–orbit coupling mixes the spin of the Landau band[20,28,35], which enables the spin-flipped T_α and T_γ transition at $B > B_1$ and also explains the absence of T_0 splitting at $B < B_1$ as summarized in Table 1. To extract the B_1 value, we perform a multi-peak Lorentz fitting on the magneto-absorbance spectrum and extract the peak position of T_α and T_β as shown in Fig. 3a(iv). The splitting feature is confirmed and agrees with the model given by the solid lines. The intersecting magnetic field gives $B_1 \approx 4.5$ T. Details of T_0 transitions including the intensity distribution, field-dependent spin mixing and multi-peak Lorentz fitting are given in Supplementary Sections III and XI. The energy of the intra-band transition $L^-_{+0} \to L^-_{+1}$ is close to that of the inter-band transition $L^+_{-0} \to L^+_{+1}$ after the system reaches the quantum limit, and therefore they merge in T_0. Previous studies[35,43] have discussed a picture of Landau levels with band edge touching in $ZrTe_5$ using a strong TI model or

Table 1 | Optical transition activity at different field-driven phases

Magnetic field	$T_{\alpha1}$	$T_{\alpha2}$	$T_{\beta1}$	$T_{\beta2}$	$T_{\beta1}$*	$T_{\beta2}$*	$T_{\gamma1}$	$T_{\gamma2}$
	$L^+_{-0} \to L^-_{+1}$	$L^+_{-1} \to L^-_{+0}$	$L^-_{+0} \to L^-_{+1}$	$L^+_{-1} \to L^+_{-0}$	$L^+_{-0} \to L^+_{+1}$	$L^-_{-1} \to L^-_{+0}$	$L^-_{+0} \to L^+_{+1}$	$L^-_{-1} \to L^+_{-0}$
0–B_0	×	×	×	×	×	×	×	×
B_0–B_1	×	×	✓	×	✓	×	×	×
B_1–B_2	✓	×	✓	×	✓	×	✓	×
B_2	×	×	✓	✓	×	×	✓	✓

assuming a fixed Fermi energy. Their model gives a distinct k_z dispersion variation and Fermi level variation, as discussed below.

We note that the position of the Fermi level is vital to determine the optical activity of the transitions beyond the quantum limit for $HfTe_5$. In 2D systems, the Landau levels are non-dispersive so that the Fermi level ultimately stays exactly at the lowest level of occupied bands. However, for 3D systems, the dispersion along the field direction of the Landau bands may shift the Fermi level away from the Landau band energy at $k_z = 0$. In a 3D trivial insulator, the Fermi level always stays higher than L_{+0} but gradually converges to its band extrema due to the increasing DOS with magnetic fields (Fig. 3b, left panel). For a strong TI, the Fermi level first decreases with magnetic field followed by an upturn (Fig. 3b, middle panel), since the system becomes fully gapped again after the band edge touching. As for a weak 3D TI, the Fermi level continues to drop after the band edge touching due to the persistent gap closure (Fig.3b, right panel). The dispersion of zeroth Landau bands along k_z can be directly obtained from the proposed Hamiltonian $E_0^s(k_z) = -s(\Delta + M/l_B^2) + M_z k_z^2$ (More details in the Methods). The effect of the Fermi level shifting with fields has been mostly overlooked in previous studies of the $ZrTe_5$ or $HfTe_5$ Landau level spectrum. Below, we will show that Landau level transitions in $HfTe_5$ can be explained well by this picture.

Generally speaking, the optical transition activity of T_0 persists beyond the quantum limit, and the intensity grows with fields, since the Fermi level no longer crosses any Landau band edge. However, as indicated by the bottom orange arrow in Fig. 2f, T_α becomes weakened and gradually disappears above $B_2 \approx 21$ T, while all other T_0 transitions get enhanced. Figure 3a(ii),(iii),(v) also clearly indicates the reduction of T_α. This striking phenomenon contrasts the traditional argument and suggests that the Fermi level further crosses L^+_{-0} around B_2. Above B_2, the emptying of L^+_{-0} forbids all transitions initializing from L^+_{-0} (Fig. 3c), and hence T_α vanishes accordingly. By contrast, T_β and T_γ persist above B_2. Figure 3c shows the assigned transitions for T_β and T_γ. The subscript numbers '1' and '2' denote the optical transition with opposite circular polarization. $T_{\beta1}$ and $T_{\beta2}$ are intra-band transitions after B_1, while $T_{\beta1}$* and $T_{\beta2}$* are inter-band transitions. While $T_{\beta1}$ (solid dark green) maintains the optical activity through B_2, $T_{\beta2}$ (dashed dark green) becomes active, resulting in the increased overall intensity of T_β above B_2. By comparison, $T_{\beta1}$* (solid light green) experiences similar variation as $T_{\alpha1}$, but is at the same energy as T_β. Considering the spin conservation nature and the overlapping of $T_{\beta1,2}$ and $T_{\beta1}$*, T_β shows the highest intensity among the T_0 transitions. The remaining T_γ transition naturally comes with the highest energy of the transition $L^-_{+0} \to L^+_{+1}$. With a similar argument, while $T_{\gamma1}$ remains active through B_2, the $T_{\gamma2}$ transition is expected to appear only after B_2, where the increased intensity and broadening of T_γ are observed (the upper orange arrow in Fig. 2f). Due to the level broadening effect from disorder and finite temperature, the discussed optical activity variation will not change abruptly but will gradually fade away. To quantitatively analyse the optical activity variation of T_α, we perform the multi-peak Lorentz fitting to extract the Pauli-blocking-induced normalized spectral weight (SW_{PB}) variation as shown in Fig. 3a(v) (fitting details and model predictions are presented in Supplementary Sections III and XI). The SW_{PB} of T_α is expected to decrease most steeply around B_2. Therefore, the extreme point of its first derivative gives the critical field $B_2 \approx 21$ T. Meanwhile, the fitted peak width is found to increase with magnetic field, indicating the presence of impurity scattering[44–46].

These observations suggest that the as-grown $HfTe_5$ is indeed a weak 3D TI. The experimental data can be fitted well by the **k · p** model with the band parameters given in Supplementary Section IV. To further verify the consistency between the experimental results and our model, we reproduce the magneto-optical conductivity spectrum with fitting parameters as shown in Fig. 3d. The observed spectrum is well reproduced, as is the overall topological phase transitions throughout the magnetic field range. The optical activity of the T_0 transition is summarized in Table 1. We also discuss the discrepancy between $ZrTe_5$ and $HfTe_5$ in Supplementary Section V.

After the topological Lifshitz transition at B_2, two spin-polarized Landau bands cross near the Fermi level, analogue to the 3D Weyl node formed by Bloch band crossing. Under high magnetic fields, the low-energy excitation resembles effective 1D Weyl quasiparticles because the Landau bands disperse only along k_z. Moreover, the Fermi velocity of the obtained 1D Weyl mode can be tuned from 5×10^4 m s^{-1} at $B_2 \approx 21$ T to 7×10^4 m s^{-1} at the highest experimental field of 35 T. The theoretically allowed Fermi velocity is expected to reach ~2×10^5 m s^{-1} before annihilating the Weyl points at the boundary of the Brillouin zone around ~300 T (estimation details are given in Supplementary Sections VI and VIII).

Optical and transport response of 1D Weyl mode

The field-induced 1D Weyl mode also features a high DOS near the Fermi level. We first compare this mode with the conventional 3D Weyl node in Fig. 4a. By tuning the Fermi level through doping, the DOS near the Fermi level vanishes at the 3D Weyl node position (Fig. 4a(i)). In $HfTe_5$, the DOS of each Landau band increases with the magnetic field. As a result, higher magnetic fields push the Fermi energy towards the crossing point and increase the nearby DOS, which eventually diverges around the charge neutral point, as shown in Fig. 4a(ii).

The 1D feature of the Weyl node also gives rise to distinct electromagnetic responses compared to the one in other dimensions. For systems with linear dispersion, it is well-known that the real part of the optical conductivity follows $\sigma_1 \propto \omega^{d-2}$, where d is dimension (Fig. 4a(iii),(iv)). The Pauli blocking effect resembles the onset of this behaviour at twice the Fermi energy. The frequency-dependence of σ_1 has been fully verified in 2D and 3D massless systems such as graphene and Cd_3As_2 (refs. [47,48]). For a 3D Weyl node at finite temperature and scattering conditions, the Pauli blocking effect only mildly changes the conductivity spectrum (blue dashed line in Fig. 4a(iii)). In the 1D case, however, the divergence of optical conductivity yields a peak feature, which is exactly the case of $HfTe_5$ under a magnetic field (blue dashed line in Fig. 4a(iv)). From 1D Pauli blocking under finite temperature and scattering conditions (Fig. 4b), one can predict (1) a peak in optical conductivity with a high-energy tail, (2) that peak height increases with the fields due to the higher DOS of the Landau bands, (3) a comparatively stable frequency with magnetic fields and (4) the appearance of a peak feature after B_2. Apart from the discussed spin mixing effect in $HfTe_5$, the transition between the two zeroth Landau levels is allowed by the orbit mixing effect (Supplementary Section III contains the

https://doi.org/10.1038/s41563-022-01364-5

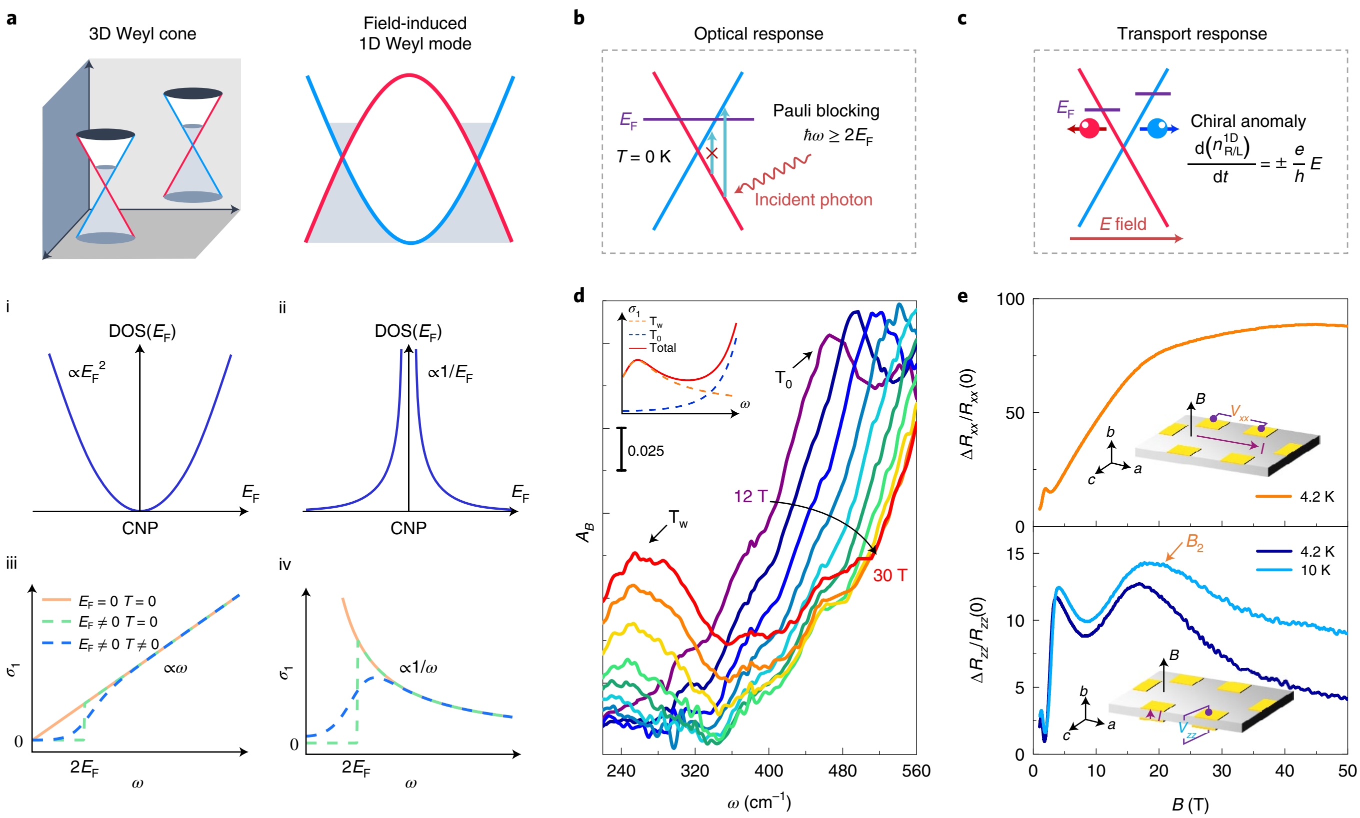

Fig. 4 | Signature of 1D Pauli blocking and chiral anomaly. a, Comparison between 3D Weyl cone and field-induced 1D Weyl mode. The upper, middle and lower panels denote the comparison of band structure, the DOS near the Fermi level, and the optical conductivity with Pauli blocking, respectively. The field-induced nature of the 1D Weyl mode results in a high DOS near the Fermi level, contrasting the vanishing DOS in the 3D Weyl node. The relationship $\sigma_1 \propto \omega^{d-2}$ (d denotes the dimension) is expected for the linear band, therefore predicting a peak feature in a 1D system. CNP, charge neutral point. **b**,**c**, Schematic plots of 1D Pauli blocking and a 1D chiral anomaly as an optical and electrical (transport) response of the 1D Weyl mode, respectively. **d**, The optical conductivity at different magnetic fields. The plot shows the appearance of T_w after B_2 with a high-energy tail, increasing oscillator strength and frequency stability, consistent with 1D Pauli blocking. The inset shows a schematic spectrum for the Pauli blocking peak near the Landau level transition. **e**, Magneto-resistivity measurement. The upper panel presents the traditional in-plane Hall bar geometry. The lower panel presents the measurement with both E and B parallel to the 1D Weyl mode direction, therefore including the out-of-plane conductivity contribution after B_2.

quantitative verification) from the inversion symmetry breaking at low temperatures[30]. The complete selection rules including $\Delta|n| = 0$ and $\Delta s = \pm 2$, and the quantitative derivation are given in Supplementary Table 1 and Supplementary Section III. In the experiment, we observe a newly formed set of peaks T_w with a prominent high-energy tail above B_2, as shown in Fig. 2f and denoted by the black arrow in Fig. 4d, whose peak height increases with the fields. The presence of T_w near B_2 suggests the relation with the induced 1D Weyl mode (hence it is named T_w), but the low frequency distinguishes T_w from the T_0 transition. The typical features of T_w fit well with the 1D Pauli blocking behaviours discussed above.

For a 1D Weyl fermion, the chiral anomaly takes a simple form of $d(n^{1D}_{R/L})/dt = \pm eE/h$ where $n^{1D}_{R/L}$ denotes the number of right-handed and left-handed 1D Weyl fermions (Fig. 4c). Here E, h, e are the external electric field, Planck's constant and elementary charge, respectively. The chiral anomaly essentially describes a 1D conductivity channel. To verify the influence of the topological Lifshitz transition on the electrical properties of $HfTe_5$, we measure the electrical resistivity along the a and b axes at pulsed magnetic fields. With magnetic field applied along the b axis, longitudinal voltage V_{xx} and V_{zz} are measured with current I along a and b axes, respectively. As shown in Fig. 4e, longitudinal resistivity along a axis R_{xx} exhibits prominent linear behaviour before saturating at high fields, which may result from the impurity scattering characterized by the screened Coulomb potential (Supplementary Section X contains more discussion)[49,50]. By contrast, longitudinal resistivity along b axis R_{zz} experiences a clear drop around 20 T, which is reminiscent of the chiral-anomaly-induced negative magneto-resistivity in 3D Weyl semimetals. The critical field for negative R_{zz} is close to the field of the topological Lifshitz transition ($B_2 \approx 21$ T). Above this field, the 1D chiral anomaly gives rise to the b-axis conductive channel with chiral current proportional to E. Recall that the magnetic field increases the Landau band DOS near the Fermi level (Fig. 4a(ii)), resulting in a chiral current proportional to the magnetic fields. Consequently, field-induced 1D quasiparticles in $HfTe_5$ present a chiral anomaly with an $\mathbf{E} \cdot \mathbf{B}$-like characteristic similar to the 3D counterpart, which explains the anomalous decrease of R_{zz} above B_2 compared with R_{xx}.

In contrast with symmetry-protected topological phases such as 3D Dirac and Weyl semimetals, the 1D Weyl mode in $HfTe_5$ is not symmetry protected. Based on our magneto-infrared spectroscopy results, the gap size should be extremely small, such as a few millielectronvolts, with negligible influence in our experimental regime. The formation of the 1D Weyl mode is essentially much more difficult in a strong TI ($M < 0$, $M_z < 0$). Without spin–orbit coupling, applying quantum limit magnetic fields in a strong TI leads to the cross of the zeroth Landau bands before B_1 and a gap opening after that. Therefore, dropping the Fermi level through L_{-0} before B_1 and realizing the 1D Weyl mode near the Fermi level are not accessible, as shown in Fig. 3b. $HfTe_5$, in our case, features in-plane band inversion ($M < 0$) but an out-of-plane trivial gap ($M_z > 0$) as a weak TI. The phase transition at B_1 changes the in-plane gap to be trivial but, most importantly, turns the out-of-plane direction into a band inversion state, which guarantees a Weyl mode after B_2. The observed Landau band Lifshitz transition can be further detected by other spectroscopic techniques such as scanning tunnelling microscopy under high magnetic field, which could further verify the 1D Weyl mode and explore the electromagnetic response in real space.

Conclusion

In summary, we report the magneto-infrared spectroscopic evidence of a field-induced topological Lifshitz transition and 1D Weyl mode in $HfTe_5$. In magnetic fields, band inversion results in the inter-band Landau level crossings accompanied by the persistent closure of the bandgap. With the Fermi level further dropping with fields, the reduction in optical transitions indicates the presence of a topological Lifshitz transition and a 1D Weyl mode near the Fermi level. The observed 1D Pauli blocking behaviour and negative magneto-resistivity agree well with the electromagnetic response of the 1D Weyl fermions. The overall magneto-infrared features and field-driven phase transitions can be quantitatively explained by the TI $\mathbf{k}\cdot\mathbf{p}$ model. The realization of a 1D Weyl mode from inter-band Landau levels establishes a unified strategy of topological phase engineering.

Online content

Any methods, additional references, Nature Research reporting summaries, source data, extended data, supplementary information, acknowledgements, peer review information; details of author contributions and competing interests; and statements of data and code availability are available at https://doi.org/10.1038/s41563-022-01364-5.

References

1. Shoenberg, D. *Magnetic Oscillations in Metals* (Cambridge Univ. Press, 2009).
2. Klitzing, K. V., Dorda, G. & Pepper, M. New method for high-accuracy determination of the fine-structure constant based on quantized Hall resistance. *Phys. Rev. Lett.* **45**, 494–497 (1980).
3. Tsui, D. C., Stormer, H. L. & Gossard, A. C. Two-dimensional magnetotransport in the extreme quantum limit. *Phys. Rev. Lett.* **48**, 1559–1562 (1982).
4. Lupatini, M. et al. Spin reversal of a quantum Hall ferromagnet at a Landau level crossing. *Phys. Rev. Lett.* **125**, 067404 (2020).
5. Jungwirth, T. & MacDonald, A. H. Pseudospin anisotropy classification of quantum Hall ferromagnets. *Phys. Rev. B* **63**, 035305 (2000).
6. Ferreira, G. J., Freire, H. J. P. & Egues, J. C. Many-body effects on the ρ_{xx} ringlike structures in two-subband wells. *Phys. Rev. Lett.* **104**, 066803 (2010).
7. Taychatanapat, T., Watanabe, K., Taniguchi, T. & Jarillo-Herrero, P. Quantum Hall effect and Landau-level crossing of Dirac fermions in trilayer graphene. *Nat. Phys.* **7**, 621–625 (2011).
8. Das, I. et al. Symmetry-broken Chern insulators and Rashba-like Landau-level crossings in magic-angle bilayer graphene. *Nat. Phys.* **17**, 710–714 (2021).
9. Weyl, H. Gravitation and the electron. *Proc. Natl Acad. Sci. USA* **15**, 323–334 (1929).
10. Wan, X., Turner, A. M., Vishwanath, A. & Savrasov, S. Y. Topological semimetal and Fermi-arc surface states in the electronic structure of pyrochlore iridates. *Phys. Rev. B* **83**, 205101 (2011).
11. Weng, H., Fang, C., Fang, Z., Bernevig, B. A. & Dai, X. Weyl semimetal phase in noncentrosymmetric transition-metal monophosphides. *Phys. Rev. X* **5**, 011029 (2015).
12. Lv, B. Q. et al. Experimental discovery of Weyl semimetal TaAs. *Phys. Rev. X* **5**, 031013 (2015).
13. Xu, S. Y. et al. Discovery of a Weyl fermion semimetal and topological Fermi arcs. *Science* **349**, 613–617 (2015).
14. Morali, N. et al. Fermi-arc diversity on surface terminations of the magnetic Weyl semimetal $Co_3Sn_2S_2$. *Science* **365**, 1286–1291 (2019).
15. Huang, X. et al. Observation of the chiral-anomaly-induced negative magnetoresistance in 3D Weyl semimetal TaAs. *Phys. Rev. X* **5**, 031023 (2015).
16. Zhang, C. et al. Room-temperature chiral charge pumping in Dirac semimetals. *Nat. Commun.* **8**, 13741 (2017).
17. Suzuki, T. et al. Large anomalous Hall effect in a half-Heusler antiferromagnet. *Nat. Phys.* **12**, 1119–1123 (2016).
18. Zhang, C. et al. Quantum Hall effect based on Weyl orbits in Cd_3As_2. *Nature* **565**, 331–336 (2019).
19. Yuan, X. et al. The discovery of dynamic chiral anomaly in a Weyl semimetal NbAs. *Nat. Commun.* **11**, 1259 (2020).
20. Chen, R. Y. et al. Magnetoinfrared spectroscopy of Landau levels and Zeeman splitting of three-dimensional massless Dirac fermions in $ZrTe_5$. *Phys. Rev. Lett.* **115**, 176404 (2015).
21. Ma, Q. et al. Direct optical detection of Weyl fermion chirality in a topological semimetal. *Nat. Phys.* **13**, 842–847 (2017).
22. Yuan, X. et al. Chiral Landau levels in Weyl semimetal NbAs with multiple topological carriers. *Nat. Commun.* **9**, 1854 (2018).
23. Wu, L. et al. Giant anisotropic nonlinear optical response in transition metal monopnictide Weyl semimetals. *Nat. Phys.* **13**, 350–355 (2017).
24. Polatkan, S. et al. Magneto-optics of a Weyl semimetal beyond the conical band approximation: case study of TaP. *Phys. Rev. Lett.* **124**, 176402 (2020).
25. Volovik, G. E. Topological Lifshitz transitions. *Low. Temp. Phys.* **43**, 47–55 (2017).
26. Bernevig, B. A., Hughes, T. L. & Zhang, S.-C. Quantum spin Hall effect and topological phase transition in HgTe quantum wells. *Science* **314**, 1757–1761 (2006).
27. Jiang, Y. et al. Unraveling the topological phase of $ZrTe_5$ via magneto-infrared spectroscopy. *Phys. Rev. Lett.* **125**, 046403 (2020).
28. Jiang, Y. et al. Landau-level spectroscopy of massive Dirac fermions in single-crystalline $ZrTe_5$ thin flakes. *Phys. Rev. B* **96**, 041101 (2017).
29. You, L., Zhang, Z.-Y. & Wang, Y.-X. Magneto-optic signatures in the gapped Dirac semimetal with mixed linear and parabolic dispersions of $ZrTe_5$. *New J. Phys.* **23**, 123033 (2021).
30. Wang, Y. et al. Gigantic magnetochiral anisotropy in the topological semimetal $ZrTe_5$. *Phys. Rev. Lett.* **128**, 176602 (2022).
31. Weng, H., Dai, X. & Fang, Z. Transition-metal pentatelluride $ZrTe_5$ and $HfTe_5$: a paradigm for large-gap quantum spin Hall insulators. *Phys. Rev. X* **4**, 011002 (2014).
32. Monserrat, B. & Narayan, A. Unraveling the topology of $ZrTe_5$ by changing temperature. *Phys. Rev. Res.* **1**, 033181 (2019).
33. Morice, C., Lettl, E., Kopp, T. & Kampf, A. P. Optical conductivity and resistivity in a four-band model for $ZrTe_5$ from *ab initio* calculations. *Phys. Rev. B* **102**, 155138 (2020).
34. Wang, H. et al. Discovery of log-periodic oscillations in ultraquantum topological materials. *Sci. Adv.* **4**, eaau5096 (2018).
35. Chen, Z.-G. et al. Spectroscopic evidence for bulk-band inversion and three-dimensional massive Dirac fermions in $ZrTe_5$. *Proc. Natl Acad. Sci. USA* **114**, 816–821 (2017).
36. Tang, F. et al. Three-dimensional quantum Hall effect and metal–insulator transition in $ZrTe_5$. *Nature* **569**, 537–541 (2019).
37. Martino, E. et al. Two-dimensional conical dispersion in $ZrTe_5$ evidenced by optical spectroscopy. *Phys. Rev. Lett.* **122**, 217402 (2019).
38. Qin, F. et al. Theory for the charge-density-wave mechanism of 3D quantum Hall effect. *Phys. Rev. Lett.* **125**, 206601 (2020).
39. Zhang, C. et al. Magnetic-field-induced nonlinear transport in $HfTe_5$. *Natl Sci. Rev*. https://doi.org/10.1093/nsr/nwab208 (2021).

40. Zhang, Y. et al. Electronic evidence of temperature-induced Lifshitz transition and topological nature in $ZrTe_5$. *Nat. Commun.* **8**, 15512 (2017).
41. Xu, B. et al. Temperature-driven topological phase transition and intermediate Dirac semimetal phase in $ZrTe_5$. *Phys. Rev. Lett.* **121**, 187401 (2018).
42. Kamm, G., Gillespie, D., Ehrlich, A., Peebles, D. & Levy, F. Fermi surface, effective masses, and energy bands of $HfTe_5$ as derived from the Shubnikov–de Haas effect. *Phys. Rev. B* **35**, 1223–1229 (1987).
43. Zhang, J. L. et al. Anomalous thermoelectric effects of $ZrTe_5$ in and beyond the quantum limit. *Phys. Rev. Lett.* **123**, 196602 (2019).
44. Cai, W. & Ting, C. S. Screening effect on the Landau-level broadening for electrons in GaAs-$Ga_{1-x}Al_xAs$ heterojunctions. *Phys. Rev. B* **33**, 3967–3972 (1986).
45. Jiang, Z. et al. Infrared spectroscopy of Landau levels of graphene. *Phys. Rev. Lett.* **98**, 197403 (2007).
46. Han, X., Salehi, M., Oh, S. & Wu, L. A new type of cyclotron resonance from charge-impurity scattering in the bulk-insulating Bi_2Se_3 thin films. *J. Phys. Appl. Phys.* **55**, 364004 (2022).
47. Akrap, A. et al. Magneto-optical signature of massless Kane electrons in Cd_3As_2. *Phys. Rev. Lett.* **117**, 136401 (2016).
48. Mak, K. F. et al. Measurement of the optical conductivity of graphene. *Phys. Rev. Lett.* **101**, 196405 (2008).
49. Abrikosov, A. A. Quantum magnetoresistance. *Phys. Rev. B* **58**, 2788–2794 (1998).
50. Rodionov, Y. I., Kugel, K. I., Aronzon, B. A. & Nori, F. Effect of disorder on the transverse magnetoresistance of Weyl semimetals. *Phys. Rev. B* **102**, 205105 (2020).

https://doi.org/10.1038/s41563-022-01364-5

Methods

Material choice and crystal preparation

$HfTe_5$ is chosen to achieve the proposed 1D Weyl mode due to its low Fermi energy, accessible quantum limit and location at the strong/weak TI phase boundary[51–62]. The $HfTe_5$ single crystals were prepared by the standard chemical vapour transport method. Stoichiometric mixtures of Hf and Te powder were sealed in an evacuated quartz tube. Iodine was added as the transport agent. The tube was placed in a two-zone furnace with a hot end temperature setting at 770 K and a temperature gradient of 100 K. After reaching the designed temperature, the condition was held for two weeks. Needle-like single crystals were obtained after cooling to room temperature.

Magneto-infrared measurement

Magneto-infrared spectroscopy was performed using a Fourier-transform infrared (FTIR) spectrometer (Bruker IFS-66) with a 35 T resistive magnet at the National High Magnetic Field Laboratory, Tallahassee. The collimated infrared beam from the spectrometer was propagating inside an evacuated beamline and focused at the top of the probe with a diamond window. Then the infrared beam was guided through a brass light pipe to the sample space, which was cooled to liquid helium temperature by a small amount of helium exchange gas. The thin $HfTe_5$ flakes with a thickness of tens of micrometres were mechanically exfoliated from the bulk $HfTe_5$ single crystals. After mounting them on the transmission sample holder, a d.c. magnetic field was applied along the crystallographic *b* axis in the Faraday geometry. The infrared beam went through the sample and then was detected by a 4.2 K composite silicon bolometer located just a short distance below. The single transmission spectra were collected with an acquisition time of about 3 min.

Magneto-transport measurement

Low-field magneto-transport measurements were carried out using a superconducting magnet with a standard lock-in technique. High-field magneto-transport measurements were performed in a pulsed magnet of up to 50 T.

The k · p model of $HfTe_5$

The ideal Hamiltonian of $HfTe_5$ is given by Eq. (1); when applying a magnetic field B along the z axis, the energy of the Landau bands in the TI are as follows:

$$E_n^s(k_z=0) = -s\frac{M}{l_B^2} + \alpha\sqrt{\left(\Delta + 2\frac{M}{l_B^2}|n|\right)^2 + 2\frac{\hbar^2\bar{v}_F^2}{l_B^2}|n|}, n = \pm1, \pm2, \pm3\ldots, \quad (2)$$

$$E_{n=0}^s(k_z=0) = -s\left(\Delta + \frac{M}{l_B^2}\right), \quad (3)$$

$$E_{n=0}^s(k_z) = -s\left(\Delta + \frac{M}{l_B^2}\right) + M_z k_z^2, \quad (4)$$

where $\bar{v}_F = \sqrt{v_{Fx}v_{Fy}}$ and n, $\alpha = \pm1$ and $s = \pm1$ denote the Landau index, carrier type index and spin index, respectively; $l_B = \sqrt{\hbar/eB}$ is the magnetic length. The optical transitions between Landau levels in the ideal case generally follow selection rules of $\Delta|n| = \pm1$. Therefore, the optical transitions occur from both $L_{-n} \to L_{n+1}$ and $L_{-(n+1)} \to L_n$, where L_n denotes the nth Landau level. The optical transitions at $k_z = 0$ require a photon energy of

$$\omega(n,B) = \sqrt{\left[\Delta + 2\frac{M}{l_B^2}(|n|+1)\right]^2 + 2\frac{\hbar^2\bar{v}_F^2}{l_B^2}(|n|+1)} + \sqrt{\left(\Delta + 2\frac{M}{l_B^2}|n|\right)^2 + 2\frac{\hbar^2\bar{v}_F^2}{l_B^2}|n|}. \quad (5)$$

Detailed discussions including the Zeeman effect[63], disorder[64–67] and other perturbation terms are provided in Supplementary Sections III and X.

Data availability

Source data are provided with this paper. All other supporting data are available from the corresponding authors upon reasonable request.

References

51. Chen, R. et al. Optical spectroscopy study of the three-dimensional Dirac semimetal $ZrTe_5$. *Phys. Rev. B* **92**, 075107 (2015).
52. Liu, Y. et al. Zeeman splitting and dynamical mass generation in Dirac semimetal $ZrTe_5$. *Nat. Commun.* **7**, 12516 (2016).
53. Galeski, S. et al. Unconventional Hall response in the quantum limit of $HfTe_5$. *Nat. Commun.* **11**, 5926 (2020).
54. Zhao, P.-L., Lu, H.-Z. & Xie, X. C. Theory for magnetic-field-driven 3D metal-insulator transitions in the quantum limit. *Phys. Rev. Lett.* **127**, 046602 (2021).
55. Fu, B., Wang, H.-W. & Shen, S.-Q. Dirac polarons and resistivity anomaly in $ZrTe_5$ and $HfTe_5$. *Phys. Rev. Lett.* **125**, 256601 (2020).
56. Choi, Y., Villanova, J. W. & Park, K. Zeeman-splitting-induced topological nodal structure and anomalous Hall conductivity in $ZrTe_5$. *Phys. Rev. B* **101**, 035105 (2020).
57. Wang, C. Thermodynamically induced transport anomaly in dilute metals $ZrTe_5$ and $HfTe_5$. *Phys. Rev. Lett.* **126**, 126601 (2021).
58. Zheng, G. et al. Field-induced topological phase transition from a three-dimensional Weyl semimetal to a two-dimensional massive Dirac metal in $ZrTe_5$. *Phys. Rev. B* **96**, 121401 (2017).
59. Liang, T. et al. Anomalous Hall effect in $ZrTe_5$. *Nat. Phys.* **14**, 451–455 (2018).
60. Xiong, H. et al. Three-dimensional nature of the band structure of $ZrTe_5$ measured by high-momentum-resolution photoemission spectroscopy. *Phys. Rev. B* **95**, 195119 (2017).
61. Zhang, Y. et al. Temperature-induced Lifshitz transition in topological insulator candidate $HfTe_5$. *Sci. Bull.* **62**, 950–956 (2017).
62. Li, Q. et al. Chiral magnetic effect in $ZrTe_5$. *Nat. Phys.* **12**, 550–554 (2016).
63. Büttner, B. et al. Single valley Dirac fermions in zero-gap HgTe quantum wells. *Nat. Phys.* **7**, 418–422 (2011).
64. Klier, J., Gornyi, I. V. & Mirlin, A. D. Transversal magnetoresistance in Weyl semimetals. *Phys. Rev. B* **92**, 205113 (2015).
65. Pesin, D. A., Mishchenko, E. G. & Levchenko, A. Density of states and magnetotransport in Weyl semimetals with long-range disorder. *Phys. Rev. B* **92**, 174202 (2015).
66. Xiao, X., Law, K. T. & Lee, P. A. Magnetoconductivity in Weyl semimetals: effect of chemical potential and temperature. *Phys. Rev. B* **96**, 165101 (2017).
67. Könye, V. & Ogata, M. Magnetoresistance of a three-dimensional Dirac gas. *Phys. Rev. B* **98**, 195420 (2018).

Acknowledgements

X.Y. was supported by the National Natural Science Foundation of China (grant no. 12174104, no. 62005079 and no. 62111530237), the Shanghai Sailing Program (grant no. 20YF1411700), the International Scientific and Technological Cooperation Project of Shanghai (grant no. 20520710900) and a start-up grant from East China Normal University. C.Z. was supported by the National Natural Science Foundation of China (grant no. 12174069), Shanghai Sailing Program (grant no. 20YF1402300), Natural Science Foundation of Shanghai (grant no. 20ZR1407500), the Young Scientist project of the Ministry of Education innovation platform and a start-up grant from Fudan University. H.-Z.L. was supported by the National Natural Science Foundation of China (grant no. 11925402). A portion of this work was performed at the National High Magnetic Field Laboratory, which is supported by National Science Foundation cooperative agreement no. DMR-1644779 and the State of Florida. Part of the sample fabrication was performed at Fudan Nano-fabrication Laboratory. We thank M. Orlita, M. Potemski, H. Yan, Y. Jiang, Z.-G. Chen, Z. Sun, C.-G. Duan, F. Yue, B. Tian and Y. Liu for helpful discussions.

Author contributions

X.Y. conceived the idea and supervised the overall research. X.M., B.L. and Y.M. carried out the growth of the $HfTe_5$ single crystals. M.O., W.W., Z.S. and Y.D. performed the magneto-infrared experiments. C.Z. and Y.W. conducted the magneto-transport experiments. W.W., X.Y., Z.Y., F.Q. and H.-Z.L. performed the theoretical analyses based on the $\mathbf{k}\cdot\mathbf{p}$ model. X.Y., W.W., C.Z., Z.S. and J.C. wrote the paper with the help of all the coauthors.

Competing interests

The authors declare no competing interests.

Additional information

Supplementary information The online version contains supplementary material available at https://doi.org/10.1038/s41563-022-01364-5.

Correspondence and requests for materials should be addressed to Cheng Zhang or Xiang Yuan.

Peer review information *Nature Materials* thanks the anonymous reviewers for their contribution to the peer review of this work.